ELSEVIER

Contents lists available at ScienceDirect

Construction and Building Materials

journal homepage: www.elsevier.com/locate/conbuildmat





The influence of cement bypass dust composition on the properties of slag-based mortars

Ahmad Mahmoud Kobeiter Abiad ^{a,*}, Kypros Pilakoutas ^a, Maurizio Guadagnini ^a, Hajime Kinoshita ^b

a School of Mechanical, Aerospace and Civil Engineering, The University of Sheffield, Sir Frederick Mappin Building, Mappin Street, Sheffield S1 3JD, UK

ARTICLE INFO

Keywords: Cement mortar Bypass dust Blast furnace slag Waste utilisation Cement replacement

ABSTRACT

Research on sustainable alternatives to Ordinary Portland Cement aims to reduce global CO2 emissions from cement production. Utilizing byproducts or waste materials to create sustainable binders is a promising approach. Cement bypass dust is being investigated as a potential activator of pozzolanic materials, however there is large variability in the composition of this dust and research is necessary to understand the differences for the potential application of the waste material. The objective of this work was to compare two bypass dusts where ternary and binary mortars of bypass dust (50 %, 30 %, 10 %, 0 % and by weight), cement (100 %, 80 %, 40 % and by weight), and blast furnace slag (50 %, 30 %, 10 % and 0 % by weight), were produced. Mortars were all ambient cured and a water to binder ratio of 0.6 was maintained for all mixes. The results showed that one bypass dust had a much higher free lime and chloride content, whereas the other had more calcite and sulphates. Compressive strengths of the 1:1 slag and sulphate rich bypass dust were of 18.6 MPa at 90 days, and lime rich bypass dust achieved 15.1 MPa. X-ray diffraction and thermogravimetric analysis revealed that sulphate rich bypass dust formed more ettringite, enhancing strength, while lime rich bypass dust formed more portlandite due to its lime content. Chemical shrinkage results showed volumetric expansion at early ages for both bypass dusts with lime rich bypass dust swelling up to 0.057 ml/g and sulphate rich bypass dust up to 0.015 ml/. Despite this, both bypass dust binders exhibited higher shrinkage strains over a 150-day period compared to cement, where sulphate rich and lime rich bypass dust had strain percentages of 0.225 % and 0.228 %, respectively. This work found the main differences between the composition of two bypass dusts, and it was found that these materials can be reused to fabricate cementless binders.

1. Introduction

The production of cement is a very energy intensive process that requires the use of high temperatures (1400°C) to produce clinker [1]. Due to this, cement manufacture contributes to 8 % of global carbon dioxide emissions [2]. Hence, the construction industry is facing demand to provide more sustainable solutions to Portland cement (OPC) manufacture.

Many techniques are currently being utilised to reduce the environmental burden of the concrete industry. These include the use of recycled aggregate [3], carbon curing of concrete [4], and the use of supplementary cementitious materials as cement replacements such as granulated blast furnace slag (GBFS) [5]. GBFS is a foundational element in the formation of alkali-activated materials (AAMs), which offer a

cementless alternative for construction applications. Research on GBFS based AAMs has been well established and currently work is being undertaken to further improve the technology through techniques such as the inclusion of titanium dioxide nanoparticles[6]. GBFS has also been shown to combine with waste materials such as glass powders to make AAMs [7]. Ladle furnace slag has also been reused at cement levels of 20 % showing improvements in compressive strengths [8,9].

Additionally, several successful examples of cementless AAMs utilising waste materials have been developed in previous research. Cakmak et al. [10] developed a binder composed of obsidian and waste glass activated by 12 M sodium hydroxide as activator. Their findings showed compressive strengths of up to 52.6 MPa. Use of demolition waste as a precursor in AAMs have also been shown to be very effective [11].

Despite all the advances in AAM technology and innovation,

E-mail address: amkobeiterabiad1@sheffield.ac.uk (A.M.K. Abiad).

b School of Chemical, Materials and Biological Engineering, The University of Sheffield, Sir Robert Hadfield Building, Mappin Street, Sheffield S1 3JD, UK

^{*} Corresponding author.

challenges such as high global warming potential from chemical activators (sodium silicate), and overhaul in infrastructure, limit their widespread use into sectors like the precast industry [12]. Exploring sustainable activators from waste streams could address these challenges, offering a more environmentally friendly and cost-effective approach.

Cement bypass dust (CBPD) is a waste material that has been shown to have activating potential of GBFS [13]. Due to an increase in the use of alternative fuels in the cement kiln has led to the need of implementing a bypass system in most modern kilns [14]. CBPD is formed during the manufacturing process of cement clinker. Due to its high alkali, sulphate, free lime and chloride content, this material is largely landfilled and unexploited. Cement Kiln Dust (CKD) and CBPD are often mistaken for being the same material, however they are not and have differences to each other. CKD is typically captured early in the kiln system, where it is captured by exhaust gases and is collected by electrostatic precipitators or baghouses [15]. Due to its typically stable condition, CKD is often recycled and returned to the kiln. On the other hand, CBPD is collected from the bypass system at the bottom of the kiln, where the bypass is often used to extract gasses high in chlorides and sulphates. Since CBPD is produced at much higher temperatures (1000°C), it is more calcined than CKD and contains higher levels of free lime. CBPD is much more reactive than CKD and has a higher quantity of chlorides and sulphates. Hence, for this reason CBPD is landfilled. It is important to reuse CBPD as its reuse will promote a circular economy and this is a large incentive for cement companies globally. Furthermore, CBPD has been shown to have the potential of contaminating ground water addressing this would require complicated remediation techniques [16,17]. Hence better reuse of the material is encouraged.

CBPD accounts for circa 2–5 % of the clinker production by weight [18]. This indicates that at least 80 million metric tonnes of bypass dust were produced in 2022 based clinker production statistics [19].

The chemical composition of CBPD largely changes based on the cement plant, which has been attributed in the past to the kiln type, fuel type and raw materials utilised [15]. Research comparing two types of CBPD is scarce and a large gap in knowledge exists on this subject, however there has been some work comparing two types of CKD. Chaunsali and Peethamparan [20] investigated two types of CKD on heat-cured mixes and found that the CKD with the higher free lime attained a higher strength in pozzolanic mixes. Sadique and Coakley [21] also reached the same conclusion, finding that higher sulphate and lime contents lead to stronger concretes, however admitted that due to the range in composition, further investigation was required on this material. Wojtacha-Rychter et al. [22] replaced cement by up to 30 % with CBPD and found strengths up to 51 MPa after 90 days in their concrete blocks. Gdoutos and Shah [23] compared four types of CKD. They found that the CKD with highest sulphate content formed the most ettringite and had the earliest setting time, and that its formation was also a contributor to strength. CKD has also been used in other building materials such as roof tiles [24]. Moreover, CKD has been shown to have excellent carbon sequestration potential improving the sustainability of the material [25].

Thus, the current state of the research is not enough to fully understand the differences and potential of CBPDs. Proper classification of CBPD is still required if this material is to be standardised and utilised properly in construction. Besides the sustainability potential, one of the primary benefits of using CBPD in mortars and concretes is that it does not change the manufacturing proces, where other liquid activators would.

Hence, the main of this objective of this was to compare two different types of CBPD procured from Eastern and Western Europe by using them as cement replacements in mortars. To the best of the authors knowledge, there is a lack of research on the differences between CBPD compositions and their interactions with GBFS and GBFS-OPC mortars. Additionally there is a gap in knowledge regarding the effect different compositions of CBPD have on cement-like binders. A good

understanding on the properties of different CBPDs and what can be expected from this material is lacking. Furthermore, classification of different CBPDs and their potential uses is unavailable currently. To understand the material better, the effects of CBPD composition on fresh and mechanical properties, as well as heat of hydration were investigated. In addition to this, the microstructure of CBPD-GBFS and CBPD-GBFS-OPC binders were investigated through x-ray diffraction (XRD), thermogravimetric analysis (TGA), and Fourier Transform Inrared Spectroscopy (FTIR). Finally, both the chemical and total shrinkage of these binders were observed in this experiment.

2. Experimental work

2.1. Materials

Two types of CBPD were examined, one from a cement plant in Rugby, UK, and another from a plant in Latvia, labelled as CBPD R and CBPD L, respectively. The GBFS used in this experiment was acquired from Scunthorpe, UK. The OPC used was of the CEM II type, grade 32.5 R and was procured from Hope Cement Works, Sheffield.

The mineralogical characterisation of the raw materials was determined using XRD as shown in Fig. 1. The main crystalline phases present in the CBPDs were free lime (CaO), gypsum (CaSO₄.2 $\rm H_2O$), sylvite (KCl), quartz (SiO₂), and calcite (CaCO₃).

To quantify the chemical composition of the significant phases, gypsum, calcite, sylvite and lime peak areas were calculated using peak deconvolution. The results are shown in Table 1. While both types of CBPD have similar mineralogical compositions, it is evident that CBPD L has much higher amounts of lime relative to CBPD R. On the other hand, CBPD R has a higher calcite content and sulphate (gypsum peaks) content. The alkali content in CBPD L is also higher with a pH of 13 relative to pH of 12.6 for CBPD R. OPC, as expected, is mainly composed of alite, belite, and calcite. GBFS, on the other hand, presented a very broad diffuse band indicating that it contained a very large amount of amorphous material.

The particle sizes, measured in a laser diffractometer, are shown in Fig. 2. CBPD L was the finer of the two dusts having a median particle size of 21 microns, whereas CBPD R had a median size of 46.5 microns. The smaller particle size of CBPD L will likely enable it to hydrate further due to a larger surface area. A noticeable difference between the two CBPDs was that CBPD R grains clearly agglomerated more than CBPD L, as balls of dust could easily be seen.

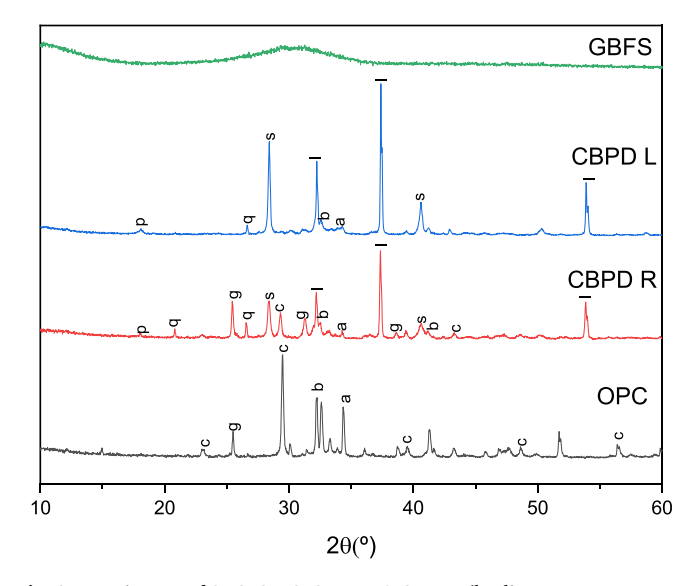


Fig. 1. XRD images of OPC, GBFS, CBPD R & CBPD L (l = lime, g = gypsum, s = sylvite, b = belite, a = alite, c = calcite, q = quartz and p = portlandite).

Table 1
Peak areas of main peaks for CBPD R and CBPD L determined using peak deconvolution.

Peak Location (2θ)	CBPD R	CBPD L
Gypsum (25 – 25.9°)	119.8	1.6
Sylvite (27.8 – 29°)	188.0	349.8
Calcite (28.9 – 29.7°)	100.1	4.3
Gypsum (30.9 – 31.7°)	86.4	24.9
Lime (31.8 – 32.4°)	114.5	195.4
Lime (37.1–37.7°)	282.3	441.9
Sylvite (40.1-40.9°)	107.6	153.0

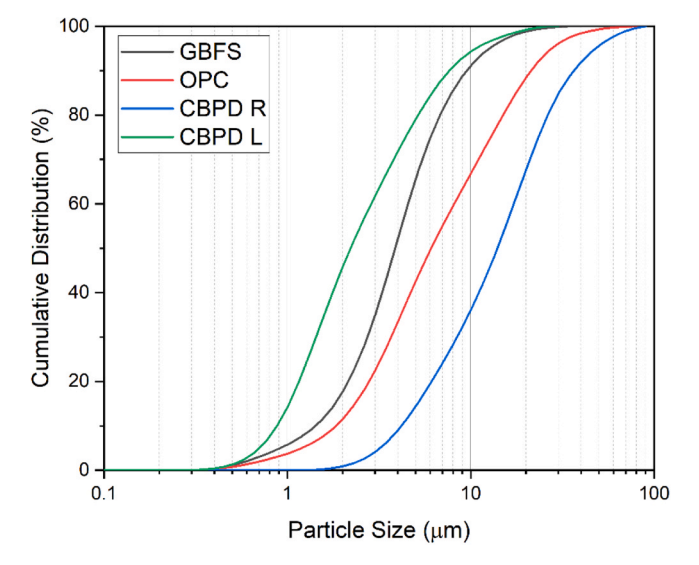


Fig. 2. Particle size of GBFS, OPC, CBPD R & CBPD L.

2.2. Specimen preparation

The mixes were designed based on the results of pilot studies. During these studies, alternative curing activation techniques such as chemical activation and heat curing were attempted, and it was found that despite a lower early age strength, ambient curing led to the strongest mixes long term. Locally available building sand was used as a fine aggregate for the mortars. The specific gravity and water absorption capacity were measured to be 2.6 and 2.5 %, respectively; these conform to the limits specified in BS EN 1097–6:2000. The binder to sand ratio was kept at 1:3. When relevant for comparison purposes, 100 % CBPD and OPC pastes at 0.4 w/b ratio were also used. Higher w/b ratios were necessary for the mortars to compensate for the sand absorption.

Seven mixes, with compositions given in Table 2, were prepared. A ratio of 50:50 of CBPD and GBFS provided the strongest paste mixes in trial tests, hence this ratio was maintained throughout the testing. Cement was then added at 40 %, 80 % to the GBFS-CBPD binder, to test the potential of cementitious binders with reduced cement content. A

Table 2 Mix Design. Sample ID: S refers to Slag, B refers to Bypass Dust. The number refers to the quantity of each (50=50 % Slag and 50 % Bypass Dust). R and L refer to CBPD from Rugby and Latvia, respectively.

Mix ID	CBPD (%)	GBFS (%)	Cement (%)	w/b ratio
SB50 R	50	50	-	0.6
SB50 L	50	50	-	0.6
SB30 R	30	30	40	0.6
SB30 L	30	30	40	0.6
SB10 R	10	10	80	0.6
SB10 L	10	10	80	0.6
OPC	-	-	100	0.6

control mix containing 100 % CEM II OPC was also tested for comparative purposes.

The binders were all mixed in a 9-litre pan-mixer. Powders were initially mixed to ensure a homogenous dry mix. Following this, the water was added, and the material was mixed for 120 seconds. After multiple trials, a water to cement ratio of 0.6 was used and this was kept constant for all mortar mixes. If dry material remained, the mortar was mixed further. Once properly mixed, the mortar was cast into steel moulds in two layers, and the surface was finished using a flat trowel. The specimens were then covered with a polyethylene sheet for 48 hours and kept in a curing room at 20 \pm 2 $^{\circ}\text{C}$ before being demoulded. Once demoulded, the mortar specimens were kept in a water curing tank also at 20 \pm 2 $^{\circ}\text{C}$ until the day of testing.

2.3. Test methods

2.3.1. Fresh properties and heat of hydration

The workability of the binders was assessed using a flow table test based on ASTM C1437. Freshly mixed mortar was cast in two layers into a conical mould. The mould was then released, and the mortar was tamped 15 times allowing it to spread out. The diameter of the mix was then measured to quantify the workability of the mix design. To measure the standard consistency, paste is cast into a mould, and different water to cement ratios are tested. The water to cement ratio which allows a Vicat plunger to penetrate a depth of 33–35 mm in the cement is the standard consistency.

Heat of hydration measurements were carried out to investigate the heat evolution of CBPD binders. Paste samples were mixed and cast into plastic bags. The total mass of the binder was 200 g per mix design. The bags were then pierced with a thermocouple so that it was in contact with the paste. This was then placed in a semi-adiabatic container and the temperature evolution over 60 hours was recorded.

2.3.2. Mechanical properties

For compressive strength $50~\text{mm}^3$ cubes were utilised, whilst for flexural strength 40x~40x160~mm prisms were used. This was following the ASTM C109 standard. To further verify the compressive strength result, the broken prism pieces from the flexural testing were also tested in compression using two $40\times40~\text{mm}$ metal plates to spread the load.

Ultrasonic Pulse Velocity (UPV) was measured using two transducers being placed at opposite ends of a prism. The UPV, denoted as V (m/s), was calculated by measuring the time (t) taken for ultrasonic pulses to go through the distance (d) of the two transducers. This is shown in the equation:

V = d/t

2.3.3. Microstructural analysis

For microstructural analysis, paste samples with a w/b ratio of 0.4 were used. The XRD of the CBPD paste samples was carried out in a Bruker D-2 diffractometer, using X-rays of 1.54 Å generated by a Cu K α target and an Ni filter. The samples were analysed from 5° to 60° at a rate of 0.02° steps per second. The software used for peak identification was Diffrac.EVA by Bruker which has an ICDD library. Origin 2022 was used for peak deconvolution of the main XRD peaks.

Thermogravimetric Analysis (TGA) was carried out using a Perkin Elmer Pyris 1 TGA. Samples were heated from 35° C to 1000° C degrees at a rate of 10° C per minute. In this study, 10 mg of the ground powder samples were used to investigate the thermal behaviour of CBPD paste.

Fourier Transform Infrared Spectroscopy (FTIR) was carried out using a Perkin Elmer Spectrometer. Potassium Bromide (KBr) pellets were formed by mixing and compressing together cementitious powder and KBr powder. The samples were measured from wavelengths $400~{\rm cm}^{-1}$ to $4000~{\rm cm}^{-1}$.

2.3.4. Shrinkage properties

The chemical shrinkage was determined following Procedure A of ASTM C1608–07. The CBPD pastes were cast into vials and compacted in 5–10 mm layers. The vials were weighed empty and filled with paste to determine the mass of the paste. Following this, they were filled with deaerated water, and sealed with rubber corks that were fitted with capillaries. Readings of the water level were taken every 30 minutes for the first 8 hours after casting, and then every 12 hours for 72 hours. The first measurement was taken 5 minutes after mixing.

Total shrinkage was carried out following ASTM C596–23. Three mortar bars were prepared for each mix design. After demoulding, the samples were water cured for 48 hours. The prisms were then removed and once they were in a saturated surface dry condition, the first length measurement was taken. The shrinkage measurements were carried out using a length comparator to quantify the linear dimension change along the longitudinal axis of the mortar bar. Shrinkage strain measurements were taken for up to 150 days.

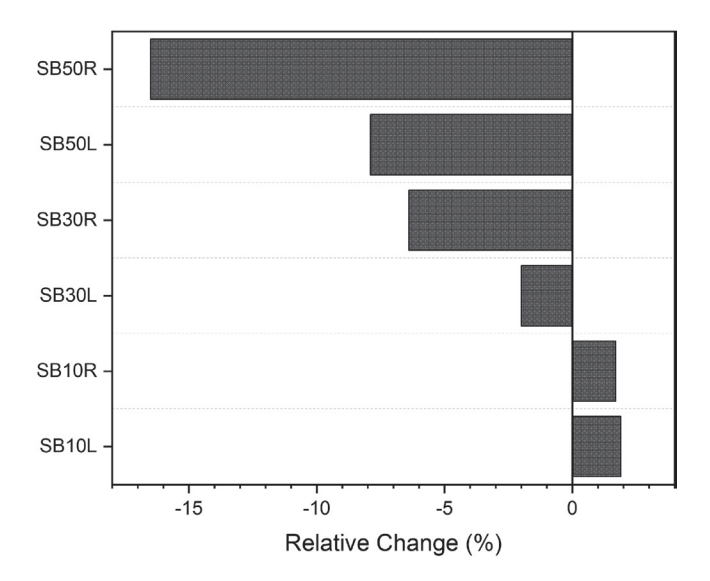
3. Results and discussion

3.1. Flow diameter, standard consistency and setting time

Using the flow table test results, the relative change in flow compared to OPC is shown in Fig. 3. Large amounts of CBPD (SB50 and SB30 mixes) clearly reduce the workability and led to a stiffer mortar at higher cement replacements. Nonetheless, some flow benefits are observed in SB10 mixes. The control mix had an overall flow diameter of 161 mm, whereas SB10R and SB10L achieved 163.1 mm and 163.5 mm respectively. The same trend is seen in the standard consistency results, shown in Table 3, where more water was required as CBPD content increased

The reduction in flowability and consistency for large amounts of CBPD is attributed to higher water demand primarily due to the tendency of CBPD particles to agglomerate together [13] and the higher alkalinity of CBPD that leads to higher reactivity.

When comparing the two CBPD mixes, CBPD L is significantly more workable than CBPD R. This is reflected in the cementless mixes, with SB50L having a flow diameter of 147.8 mm and SB50R only achieving 134.0 mm. This is likely due to the increased agglomeration in CBPD R relative to CBPD L which increases the water demand. To reduce the effect of agglomeration on rheological particles, repulsive forces, induced by adding extra water, are necessary to separate the particles from each other [26].



 $\begin{tabular}{ll} Fig. 3. Relative change in flow of mix designs containing CBPD compared to OPC. \end{tabular}$

Table 3Standard consistencies, setting times and flowability of all the investigated mix designs.

Mix Design	Standard Consistency (%)	Initial Setting (min)	Final Setting (min)	Flow Diameter (cm)
SB50R	$38~\% \pm 2~\%$	$38\pm3 \text{ min}$	$140 \pm 9 \text{ min}$	$134\pm1~\text{cm}$
SB50L	35 % \pm 1 %	$94\pm7\;min$	245 \pm	$148\pm2~cm$
			12 min	
SB30R	34 % \pm 1 %	$46\pm 3\ min$	$150\pm 8 \text{ min}$	$150\pm1~\text{cm}$
SB30L	32 % \pm 1 %	$76\pm 8 \text{ min}$	$250~\pm$	$157\pm1~\text{cm}$
			14 min	
SB10R	$28~\% \pm 2~\%$	51 ± 1 min	$155\pm4min$	$163\pm2~\text{cm}$
SB10L	$27~\% \pm 2~\%$	$63\pm2\text{min}$	$175~\pm$	$164\pm 3~\text{cm}$
			10 min	
OPC	28 % \pm 1 %	$54\pm2~\text{min}$	$160\pm 6 \text{ min}$	$161\pm1~\text{cm}$

This is also reflected in the standard consistency results, where SB50R and SB50L had consistencies of 38 % and 35 % respectively. In fact, SB30R and SB50L almost had identical results for flow and standard consistency, despite the tendency for flow to improve with cement increase. This indicates that CBPD R has a high-water demand.

Setting times are also shown in Table 3. Overall CBPD R mixes set faster than CBPD L mixes. The slower time of set of CBPD L mixes is likely due to the different chemical reactivity between the dusts.

3.2. Heat of hydration

Heat of hydration curves for CBPD R and CBPD L pastes up to 60 hours are presented in Fig. 4. The mass of the dry material was maintained at 200 g for all the pastes. The time required to reach the maximum temperature is denoted as T_{max} . CBPD L reaches T_{max} faster than CBPD R, at 21 minutes compared to 48 minutes. It must be noted that both values are very fast, indicating a high reactivity. T_{max} of 105°C is significantly higher for CBPD L than CBPD R at 74°C . The speed of reaction and temperature difference is likely largely due to the higher free lime content and fineness of CBPD L that increases the surface area for reactions. An induction period is not observed for the CBPD pastes and both seem to reach stabilisation at around 15 hours.

Czapik et al. [14] showed similar results for their CBPD analysis. A rapid heat release was experienced, followed by a rapid decrease, with no induction period. A lack of an induction period may cause difficulties during in situ casting of CBPD mortar/concrete.

Fig. 4 also includes the results for OPC, which has a small initial temperature increase, a stable induction period of about 5 hours, and a

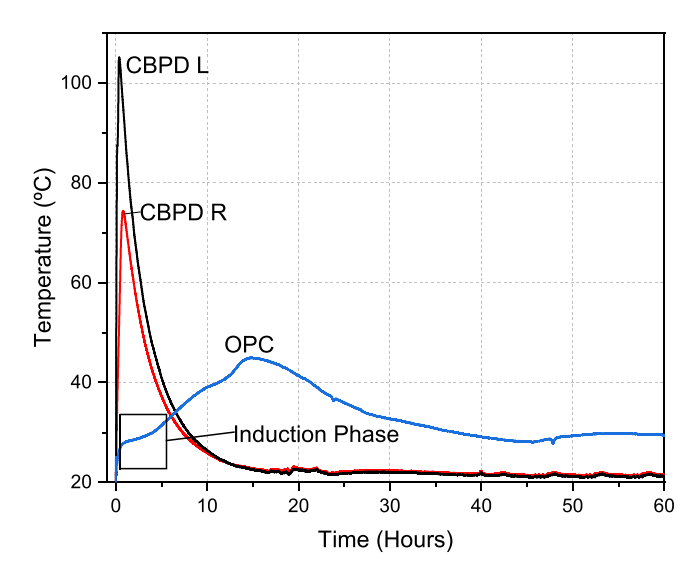


Fig. 4. Heat of hydration for CBPD R, CBPD L & OPC pastes.

gradual temperature increase where it has a T_{max} of 48°C at around 15 hours, significantly slower than the CBPD pastes.

The heat of hydration results for the investigated mortar mixes are shown in Figs. 5–7. As expected, the T_{max} decreases with an inclusion of GBFS [27]. SB50L (Fig. 5), SB30L (Fig. 6), and SB10L (Fig. 7) achieved T_{max} of 73°C, 62°C and 56°C, respectively. These values are all higher than their CBPD R counterparts and the control paste. The induction period (phase II) which occurs during cement hydration is observed only when cement is included in the binder and is labelled in the figures when present.

It is evident from the differences in the curves, that free lime hydration is the main factor governing the exothermic reaction for CBPD, whereas OPC is mainly due to C_3S . The heat of hydration of C_3S is circa -12.2 kJ/mol and for lime it is circa -64.4 kJ/mol [28].This explains why as CBPD content increases T_{max} is higher, since the heat emitted from the exothermic reaction of lime is much larger than that of C_3S . This agrees with past research on CBPD heat of hydration by Czapik et al. [14].

While CBPD L has a slaking reaction due to its lime content, it is important to highlight the difference between free lime and CBPD heat of hydration. Cai et al. [29] showed that free lime reaction with GBFS leads to a strong exothermic reaction in the first few minutes of hydration with a second peak after 18 h. Additionally, they observed rises in heat release as more lime was included in the system, which correlates with these results. Free lime is the critical factor in determining the height of the exothermic peak. In the current results, the second peak can be attributed to the delayed pozzolanic reaction and the slower reaction of free lime and GBFS [30]. In some examples, such as SB50R and SB50L, a second peak occurred in this system, however at around the 20–40-hour mark. It can be deduced that a CaO-GBFS system will dissolve GBFS faster than a CBPD-GBFS binder.

3.3. Density and ultrasonic pulse velocity

The bulk densities of the mixes after 90 days of curing are shown in Table 4. The bulk density of the mortar decreases with increasing CBPD content which may lead to a less refined and more porous the microstructure. Additionally, CBPD L leads to less dense mortars than CBPD R, which is likely due to its expansive behaviour at early ages. Expansion was clearly visible in the SB50L binders which showed surface cracks on the prisms. Excessive swelling not only affects density, but it also can increase porosity and reduce the strength of the mortar.

UPV readings (see Table 4) were taken at 90 days to verify the

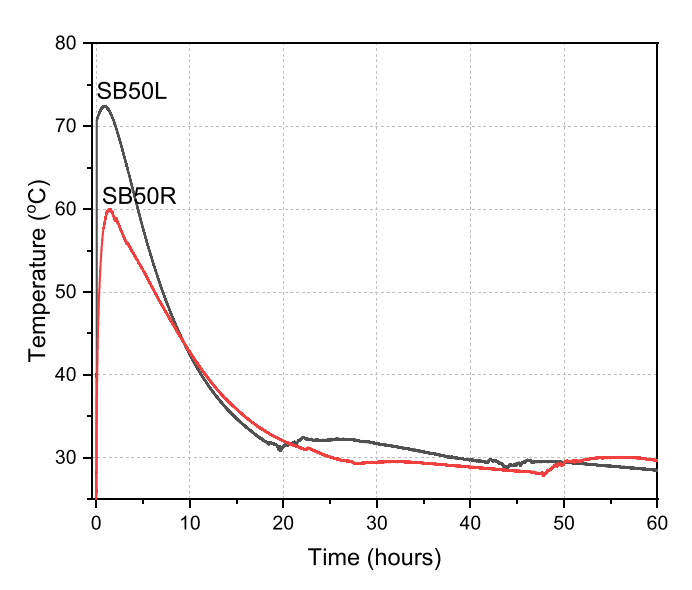


Fig. 5. Heat of hydration for SB50R and SB50L.

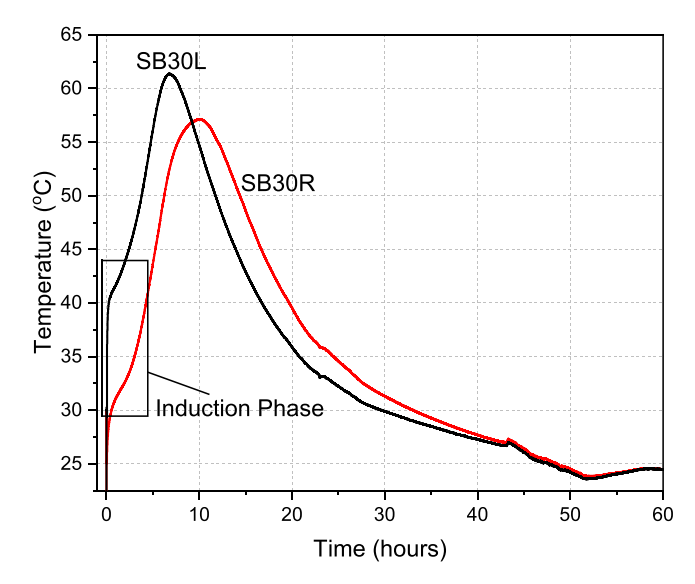


Fig. 6. Heat of hydration for SB30R and SB30L.

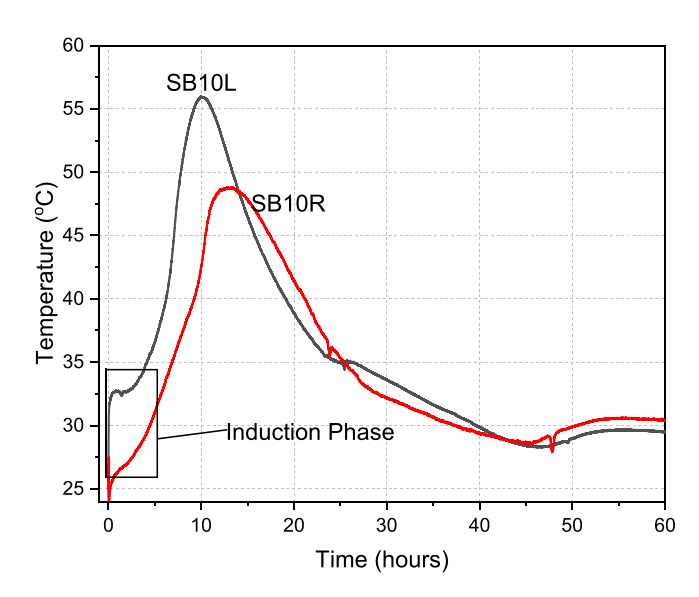


Fig. 7. Heat of hydration for SB10R and SB10L.

Table 4UPV and Density results of all the investigated binders.

Mix	Density (kg/m³)	UPV (m/s)
SB50R	2110 ± 20	3969
SB50L	2090 ± 15	3831
SB30R	2150 ± 10	4127
SB30L	2140 ± 10	4054
SB10R	2200 ± 20	4323
SB10L	2200 ± 10	4237
OPC	2210 ± 25	4304

density results. In general, the UPV results present a similar trend to densities. SB10R shows the highest velocity, but overall, the velocity decreases as CBPD increases. CBPD L mixes show the lowest velocities for the same reasons described above.

The relationship between density at 90 days and UPV is shown in Fig. 8 below. The results show a $0.99~{\rm R}^2$ value showing that there is a very strong correlation between the two properties. This correlative relationship between density and UPV is well documented in research [31].

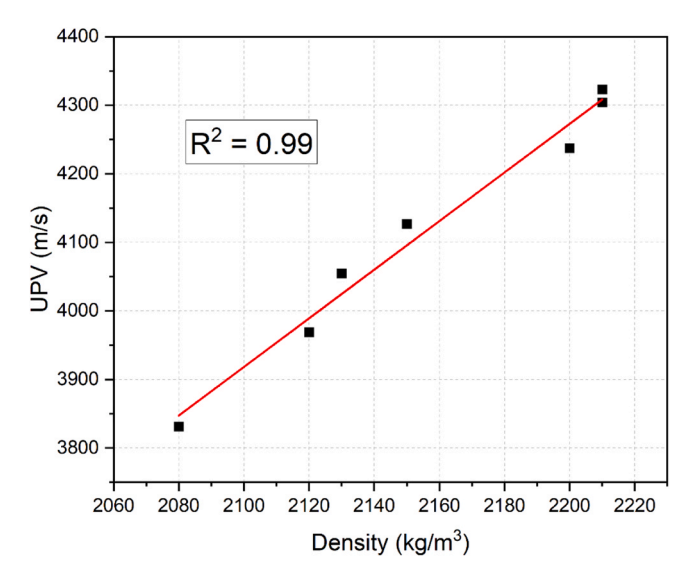


Fig. 8. Linear relationship between UPV and density showing a correlation of 99 %

3.4. Compressive and flexural strength

The average compressive strength of the mortars is shown in Fig. 9. Though CBPD L binders exhibit higher early strength (at 3 days), CBPD R produces stronger mixes over time. This is in line with the temperature vs time results, where CBPD L is shown to be more reactive than CBPD R breaking down the glassy phases of GBFS faster due to its higher exothermic reaction and alkalinity and lime content [32]. Past researchers utilised this property of CKDs to enhance the early age strength of cementitious products [21]

There are several reasons to explain the improved mechanical properties of SB50R over SB50L with time. Firstly, though it has a finer particle size, higher free lime, and alkali content, CBPD L increases early age strength, however, it appears that there is a limit to this benefit as this causes rapid expansion which can cause an uneven reaction product formation. This leads to a deterioration in the quality of the microstructure [33]. Expansion was clearly observed on CBPD L binders, hence there was also a reduction in density due to microcrack formation on the surface of the prisms. This consequently can lead to a weaker binder. Another factor contributing to the strength of CBPD binders is ettringite formation [23]. Ettringite is a mineral primarily composed of

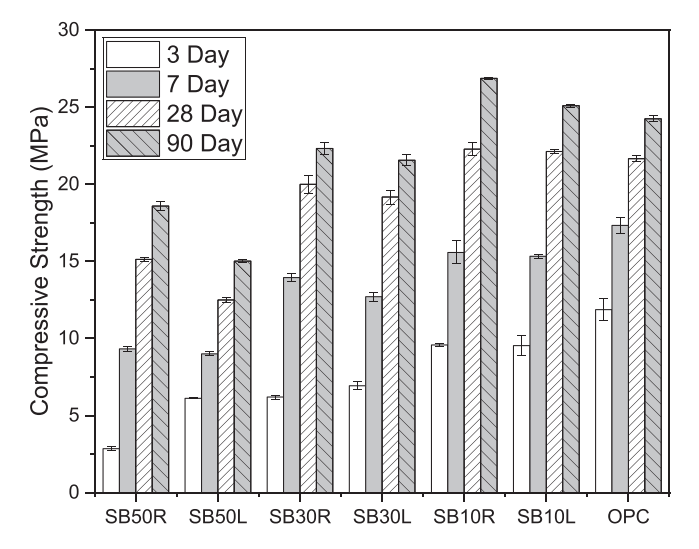


Fig. 9. Compressive strength results of all investigated mixes at 3, 7, 28 and 90 days.

sulphates and aluminates, which CBPD R is abundant in. Ettringite has a long needle shape which has an overlapping effect when formed in excess leading to improvements in the matrix strength due to pore-filling [34]. Due to the high sulphate content in CBPD, the ettringite formed tends to be quite stable. Chaunsali and Peethamparan [20] attributed much of the early age strength of their cement kiln dust-fly ash binders to the ettringite formation in their binders. Another factor to consider is the higher quantity of calcite in CBPD R is a factor contributing to the improved strength of the material. Calcite is not only denser, but it also has a larger molar volume than portlandite [35].

The highest 90-day compressive strengths were attained by SB10R and SB10L, reaching 26.1 MPa and 25.1 MPa, respectively, representing 11 % and 3 % improvements over the control mix. Good compressive strengths are achieved for SB30R and SB30L at 22.3 MPa and 21.6 MPa, respectively; these strengths were only 9 % and 13 % lower than the control mix respectively. The strength results agree with similar previous research, where Marvila et al. [36] manufactured cement-lime mortars (up to 66 % cement replacement) and achieved strengths ranging from 11.4 to 14.2 MPa at 28 days with similar w/b and binder to sand ratios as this research. Hence, these results confirm that CBPD can replace up to 10 % of typical OPC binders and still result in higher compressive strength concrete/mortar. Nonetheless, it can also be used at higher cement replacement levels up to 100 % for lower strength concrete/mortar applications.

Flexural strength obtained from three-point bending tests are shown in Fig. 10. In general, the strength develops in a similar trend to the compressive strength. SB50L was stronger in flexure at 3 days achieving 1.12 MPa whereas SB50R achieved 0.4 MPa. By 90 days, however, SB50R had exceeded SB50L's strength of 2.2 MPa achieving a flexural strength of 2.5 MPa. As is typically expected, the flexural strength at 90 days for all mixes ranged from around $10{\text -}15~\%$ of the total compressive strength. The flexural strength decreased with an increase in CBPD content.

3.5. XRD analysis

XRD is used to identify the chemical phases formed during the hydration of the pastes. Fig. 11 presents the XRD pattern for SB50R and SB50L at 7 and 28 days. At 7 days, a broad band in the range of 5–15°, attributed to the amorphous nature of CBPD, was evident, with SB50L displaying greater amorphousness than SB50R. This characteristic band diminishes by 28 days. With an increase in cement content, the amorphousness is reduced, resulting in less noise in the diffractograms, as seen in Figs. 12 and 13. While CSH typically forms broad diffusion peaks

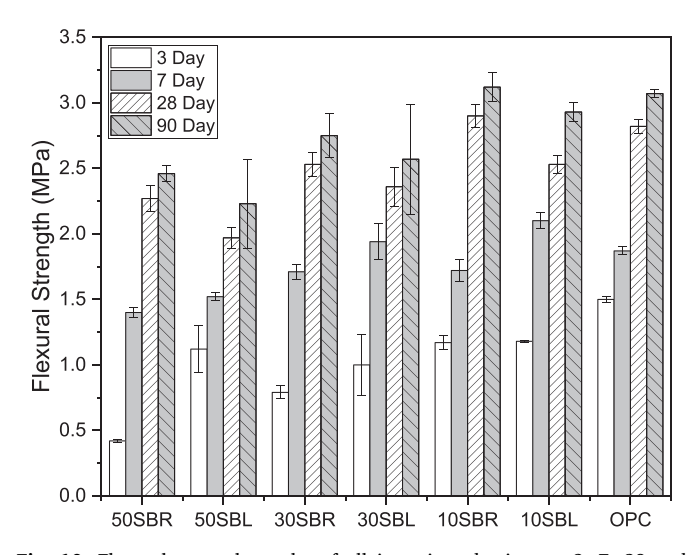


Fig. 10. Flexural strength results of all investigated mixes at 3, 7, 28 and 90 days.

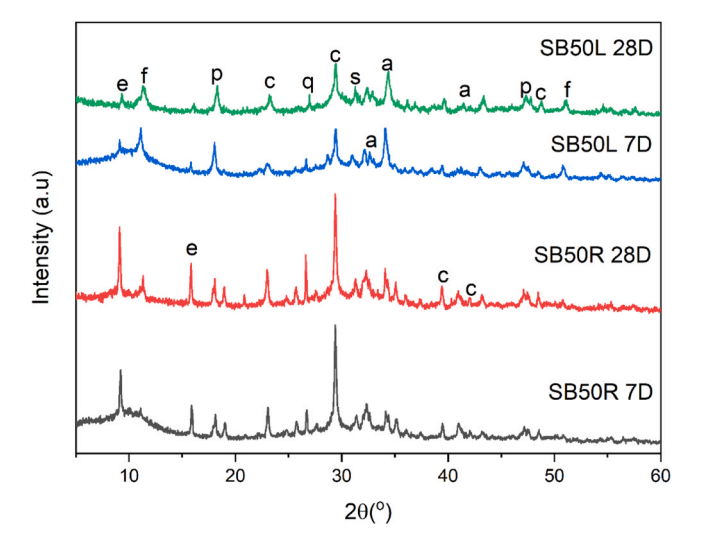


Fig. 11. XRD results of SB50R and SB50L (p = portlandite, c = calcite, e = ettringite, f = friedel's salt, a = alite, q = quartz and s = syngenite).

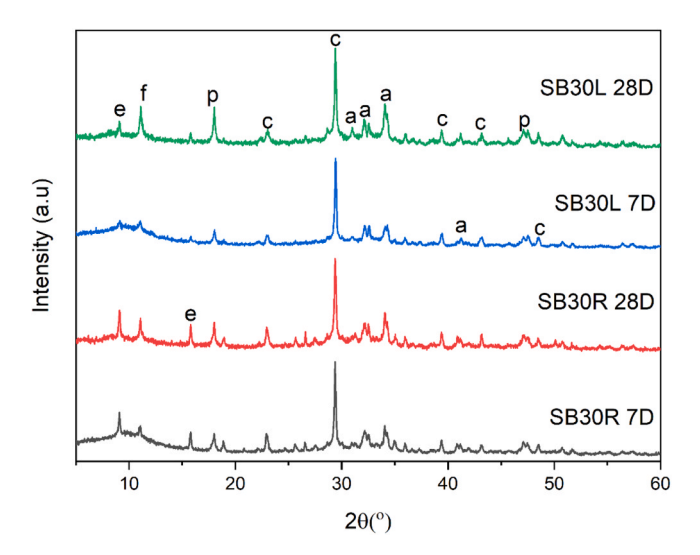


Fig. 12. XRD results of SB30R and SB30L ($p=portlandite,\ c=calcite,\ e=ettringite,\ f=friedel's$ salt and a=alite).

around 29°, these peaks are often obscured on XRD due to overlap with the major crystalline calcite peak at 29.4° [37].

Overall, both CBPDs exhibited similar phases, albeit at varying intensities due to their distinct chemical compositions. Ettringite was prominently present in these binders, with CBPD L binders showing less intense peaks, indicative of a lower quantity formed. This aligns with the strength results, where SB50R binders demonstrated greater strength than SB50L binders, underscoring the significant role of ettringite formation in strength development. CBPD R mixes produced more ettringite due to their higher sulphate content, as sulphate concentration influences ettringite formation [38]. It should be noted that the stability of ettringite is contingent on sulphate quantity; reduced amounts can lead to depletion and conversion into monosulphate (AFm) [39]. The sulphate content is sufficient as is evident in the XRD, with ettringite peaks intensifying at 28 days.

Another noticeable difference between the control and the CBPD mixes is the presence of syngenite (at 31.3°). Syngenite peaks form due to the potassium and sulphate content in the CBPD and are mostly visible in the SB50 mixes. Over time, sulphate ions from the syngenite are released and benefit the development of further ettringite [23]. The intensity of these peaks decreased as the CBPD content was reduced in

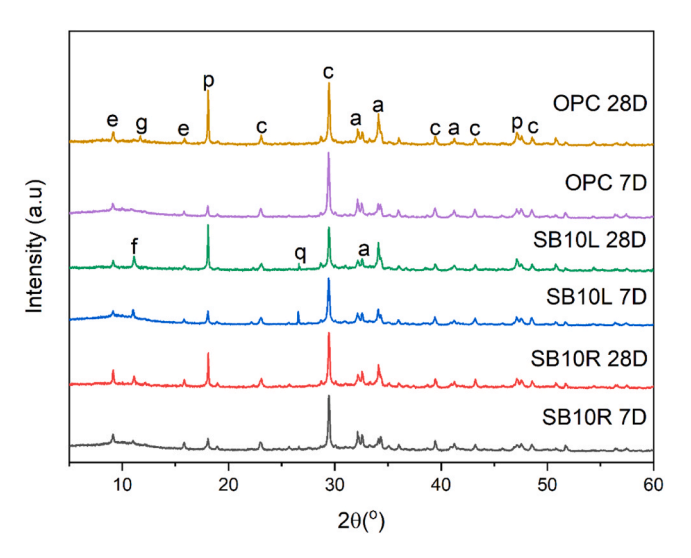


Fig. 13. XRD results of SB10R, SB10L and OPC (p= portlandite, c= calcite, e= ettringite, f= friedel's salt, a= alite, g= gypsum and q= quartz).

the binder.

Calcite peaks remained largely constant at all ages, indicating that the phase was mostly inert. On the other hand, portlandite was found in much higher concentrations in SB50L at both ages, which can be attributed to the increased free lime content in this bypass dust. Hence, it can be deduced that most of the portlandite in CBPD binders comes from the hydration of free lime. The reactivity of CBPD, dependent on free lime, sulphate, and alkali content, suggests CBPD L is more reactive. However, more reactivity and a higher portlandite content do not necessarily mean a stronger or denser product as seen from the strength results. Based on the XRD results, the ettringite content is a large determinant of overall strength. As mentioned previously, the increased calcite content is also a factor to consider due to its filling and densification effect in the binder. It is observed that at 28 days, the portlandite peak for SB50L loses intensity. This may be due to a secondary reaction between GBFS and portlandite.

The compressive strength results indicate an overall increase in strength with cement content. It is also clear from the diffractogram that the amorphous content diminishes with increasing cement content due to the orderly crystalline structure in cement. Quartz peaks were not observed in the control mix, which may be due to the lack of GBFS that contains silica. It is also possible that the samples used in the XRD did not have a high composition of quartz. SB10R and SB10L binders exhibited both enhanced fresh and mechanical properties. These mixes are characterised by higher calcite peaks (see Fig. 13) than the SB30 and SB50 mixes, consistent with the higher cement content. When observing the ettringite peaks, it is clear from the intensity that CBPD R produces the most. The inclusion of 10 % CBPD R in OPC mixes aids the quantity developed and ultimately may enhance the final compressive strength. From the diffractogram, SB10R has a higher ettringite content than OPC. The tendency of the SB10L quartz peak to decrease over time could be attributed to the formation of other cementitious gels such as CSH and CASH [40]. It can be assumed that the improved strength for SB10 mixes is due to the enhanced pozzolanic reaction of slag due to the alkalinity of CBPD.

The peak areas shown in Table 5 are obtained from semi quantitative peak quantification of the main calcite (29.4°), ettringite (9.8°), and portlandite (18.4°) peaks. OPC produces the most calcite, and there is a steady decrease in this peak as OPC content decreases, however it is also clear that calcite content is higher in CBPD R than in CBPD L, when comparing SB50R and SB50L peaks for this phase.

CBPD L binders exhibit higher portlandite production than CBPD R, primarily due to their substantial free lime content. SB50L has the highest portlandite content among all mixes at 28 days.

Table 5Main peak area ratio for all investigated mix designs at 28 days determined using peak deconvolution of main peaks.

Mix	Ettringite	Portlandite	Calcite
SB50R	162.4	106.4	290.8
SB50L	38.7	176.9	197.8
SB30R	100.8	120.5	464.6
SB30L	41.3	138.3	442.9
SB10R	93.1	148.1	693.8
SB10L	77.3	171.2	625.5
OPC	87.6	160.1	844.8

CBPD R mixes show the highest ettringite content, possibly a significant factor contributing to their improved strength results compared to CBPD L mixes. SB50R has notably higher ettringite content than the control mix, highlighting differences in hydration between pure OPC and CBPD-GBFS binders.

Based on the hydration results, a simplified hydration model was developed based on the XRD results as seen on Fig. 14. Water is added to the binder materials, and they begin to dissolve (Fig. 14 Step 1 and Step 2). An exothermic reaction results in the formation of a colloidal layer around the binder grains and free lime begins to be converted into portlandite (Fig. 14 Step 3). Ettringite also begins to form due to the reaction of sulphate ions with aluminate phases. Following this the colloidal layer thickens around the grain blocking water from the unreacted core of the grain (Fig. 14 Step 4). The binder begins to floculate and nucleate which enables more water to pass through. Hydration continues and the microstructure will densify forming a dense binder (Fig. 14 Step 5). Hydration continues over time forming more reaction product and further densifying the microstructure of the material.

3.6. FTIR analysis

Chemical phases that are difficult to locate using techniques such as XRD are easier to identify with the help of FTIR. Table 6 presents the identified IR bands and their functional groups.

The FTIR spectra of the investigated mix designs are presented in Figs. 15–17. The results show several distinct peaks typically expected in cementitious products, however, in some cases they are slightly shifted and have different intensities. The peaks located around the wavelength of $800~{\rm cm}^{-1}$ and $965~{\rm cm}^{-1}$ are due to Si-O asymmetric stretching, which occur due to the generation of CSH. This confirms that this gel forms in CBPD binders [37]. The Si-O stretching band consistently shifts to a lower wavelength in all cases, especially as cement content increases.

Table 6Functional groups classification for the FTIR results for all mix designs.

Wavenumber (cm ¹)	Functional Group
3642–3645	ν OH (Ca(OH) ₂)
2976-2980	C-H
1791796	CaCO ₃
1638-1643	δ OH (H ₂ O)
1421427	ν3 CO CaCO ₃
1131140	S-O
962–965	Si-O (CSH), Aft
873–876	C-O ν2

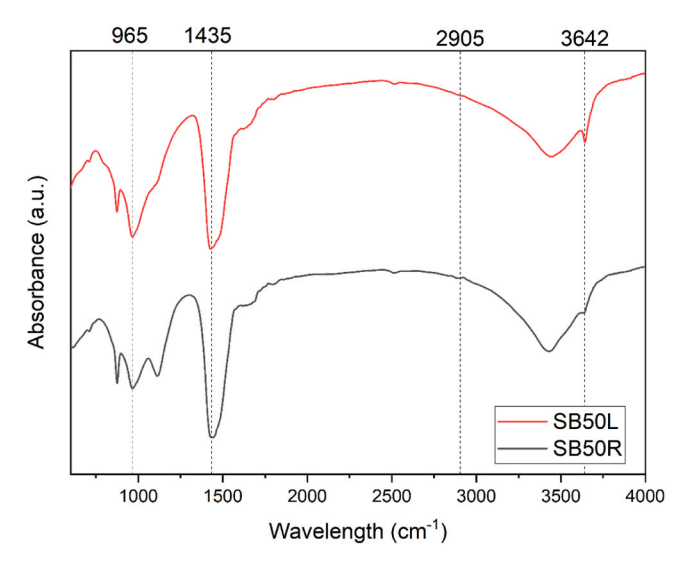


Fig. 15. FTIR results for SB50R and SB50L.

This has been reported in the past due to the progressive depolymerisation of the silicate Si-O chains. This band tends to shift to a lower frequency as the calcium/silica ratio increases in the mix [42].

CSH forms in CBPD-GBFS binders when the release of OH- ions (from the portlandite content in CBPD) in the solution break the Si-O and Al-O bonds of GBFS, forming SiO_4 and AlO_4 and releasing Ca^{2+} ions. The free calcium ions then react with the active SiO_4 and AlO_4 leading to the formation of CSH and CASH [43]. The peak around 965 cm $^{-1}$ can also indicate the presence of an ettringite and monosulphate phase that increases as CBPD content increases.

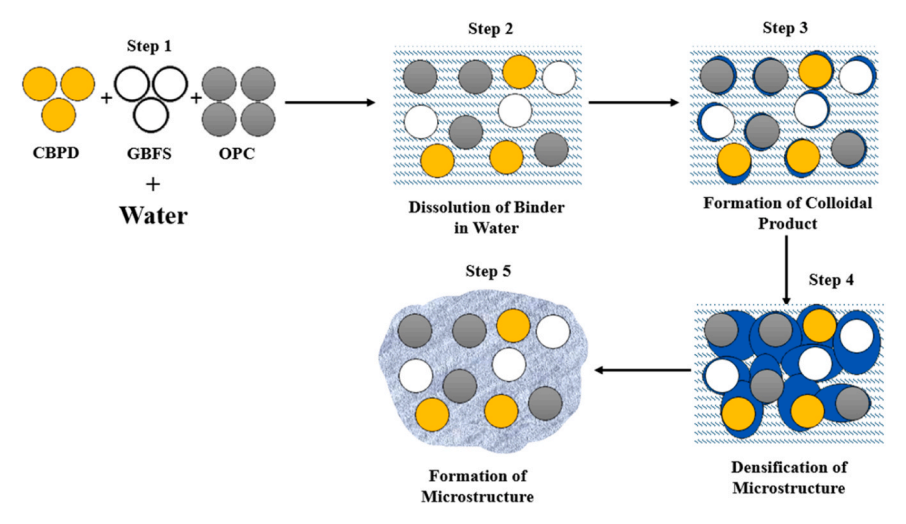


Fig. 14. Simplified hydration model of CBPD-GBFS-OPC Binders [41].

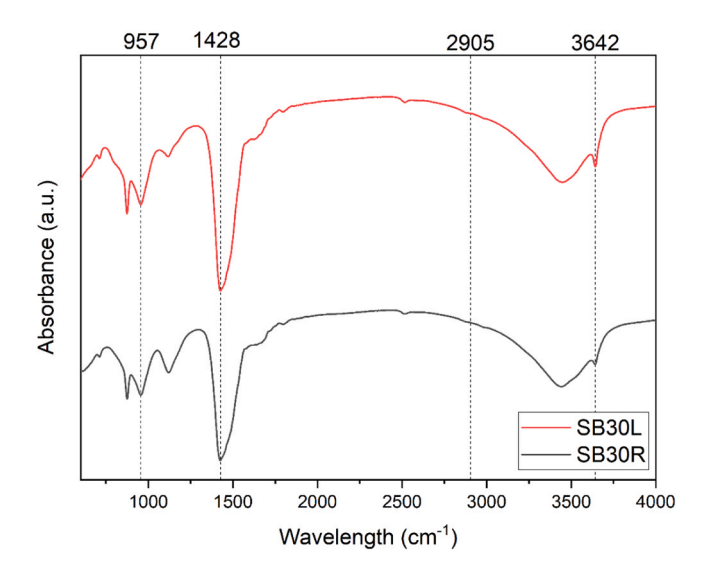


Fig. 16. FTIR results for SB30R and SB30L.

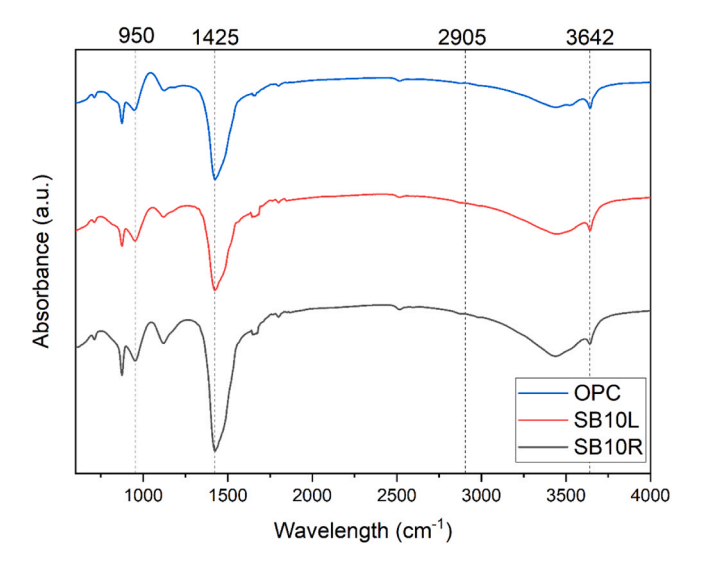


Fig. 17. FTIR results for SB10R, SB10L and OPC.

Ettringite formation can also be analysed by observing the band around $1120~{\rm cm}^{-1}$ [44]. This peak is the most intense for the mixes containing CBPD R binders, indicating more ettringite formation due to this bypass dust.

The bands located at around 1644 and 3425 cm⁻¹ occur due to the bending and stretching of bound water molecules [45]. From the results, the difference in intensities between CBPD R and CBPD L mixes are not apparent except for the SB50 mixes as seen from Fig. 15.

The band at $3642~\rm cm^{-1}$ represents an absorption peak of portlandite and is attributable to O-H stretching. The mixes containing CBPD L had higher and sharper peaks at this band relative to CBPD R, indicating more portlandite content, which confirms the XRD results. Broad bands were also observed between $3200-3400~\rm cm^{-1}$ for all mixes. This band gets broader and less sharp as the cement content increases, indicating again a lower degree of polymerisation [46].

At around 1430 cm⁻¹ a band due to the C-stretching of carbonate molecules is observed. These molecules are formed through the reaction of calcium hydroxide and carbon dioxide from the air [47]. As observed, as the cement content increases the bands slightly shift towards a lower wavelength. This indicates a higher degree of reaction in the OPC relative to the bypass dusts for calcite formation.

3.7. TGA/DTG analysis

Fig. 18 presents the TGA curves of the mixes (at 28 days) from 35° C to 1000° C. The main temperature ranges that need to be considered are between 35 and $220~^{\circ}$ C, $220-400^{\circ}$ C, $400-600~^{\circ}$ C, and $600-800~^{\circ}$ C which correspond to the loss of water and ettringite, the loss of Friedel's salt and monosulphate, the decomposition of portlandite, and the decomposition of calcium carbonate, respectively [14].

The results show that the final weight loss decreases as the CBPD content increases. The control mix experienced the greatest mass loss (23.2 %) followed closely by SB10R (22.5 %), showing that a 10 % addition of CBPD R does not significantly reduce overall reaction product formation. This mass loss is mostly the result of calcite decomposition. SB50L, had the least mass loss of 17.6 %, showing the lowest hydration products overall. Overall, CBPD L mixes show less mass loss than CBPD R mixes, confirming that they resulted in fewer hydration products. Fewer hydration products lead to a less dense matrix, weakening the binder due to less pore-filling.

Mass loss can be better understood when observing the different stages of decomposition of the mixes. The DTG results (Fig. 19) indicate that there were three distinct peaks and a weak broad peak observed in the samples, except for CBPD L samples which had four distinct peaks.

In the first phase (35–220°C), CBPD R mixes consistently exhibit the largest mass loss, indicating a higher formation of hydration products, such as ettringite and CSH. This trend holds even when compared to the control mix, emphasizing the impact of CBPD R's high sulphate content on ettringite formation, in agreement with XRD and FTIR results. From the DTG, the order of peak intensity in this phase is highest for SB50R, followed by SB30R and SB10R.

The broad band (220–400°C) corresponds to the decomposition of monosulphate and Friedel's salt. The greatest mass loss in this phase is seen in SB50L, with the mass loss reducing as the CBPD content decreased. This is because of two main factors: the presence of Friedel's salt due to the chloride content and the conversion of ettringite to monosulphate. As is evidenced from the XRD and the thermal decomposition, CBPD L mixes contain less ettringite likely due to the lower sulphate content of the dust. The Al/S ratio is imperative in the stability of ettringite, hence the reduction of sulphates in CBPD L relative to CBPD R led to the formation of monosulphate. This is also the case for the mixes containing less CBPD R which would also lead to a reduction in monosulphate phases.

When assessing the decomposition of portlandite ($400-600^{\circ}$ C) or dehydroxylation, CBPD R mixes show the lowest mass loss where SB50R only decreased by 2.3 %. On the contrary, SB50L had a mass loss of 3.5 % with a comparable value to the overall mass loss of 3.6 % for the control mix. When considering that only 50 % of the mix was composed of bypass dust for SB50 mixes, a large amount of portlandite has been formed. This was also confirmed by the XRD results which show a larger amount of portlandite for CBPD L mixes.

The final phase corresponds to the decomposition of calcium carbonate. From the results, the control mix had the largest amount of mass loss with a decrease of 8.3 %. Furthermore, CBPD R binders exhibited greater loss relative than CBPD L in each mix indicating a higher carbonate content. A significant aspect to consider is that the $CaCO_3$ decomposition of the control mix occurs at a higher temperature than mixes containing CBPD. Peaks occurring at a higher temperature indicate a more ordered $CaCO_3$ [48].

These results show the high variability in CBPD content, as CBPD R contained more $CaCO_3$ and ettringite and CBPD L contained more free lime. While increased free lime is associated with an accelerated reaction and more hydration products, excessive free lime can detrimentally impact compressive strength and structural integrity due to uneven hydration product distribution. The presence of stable and inert calcium carbonate is also identified as a significant factor in the strength of CBPD binders.

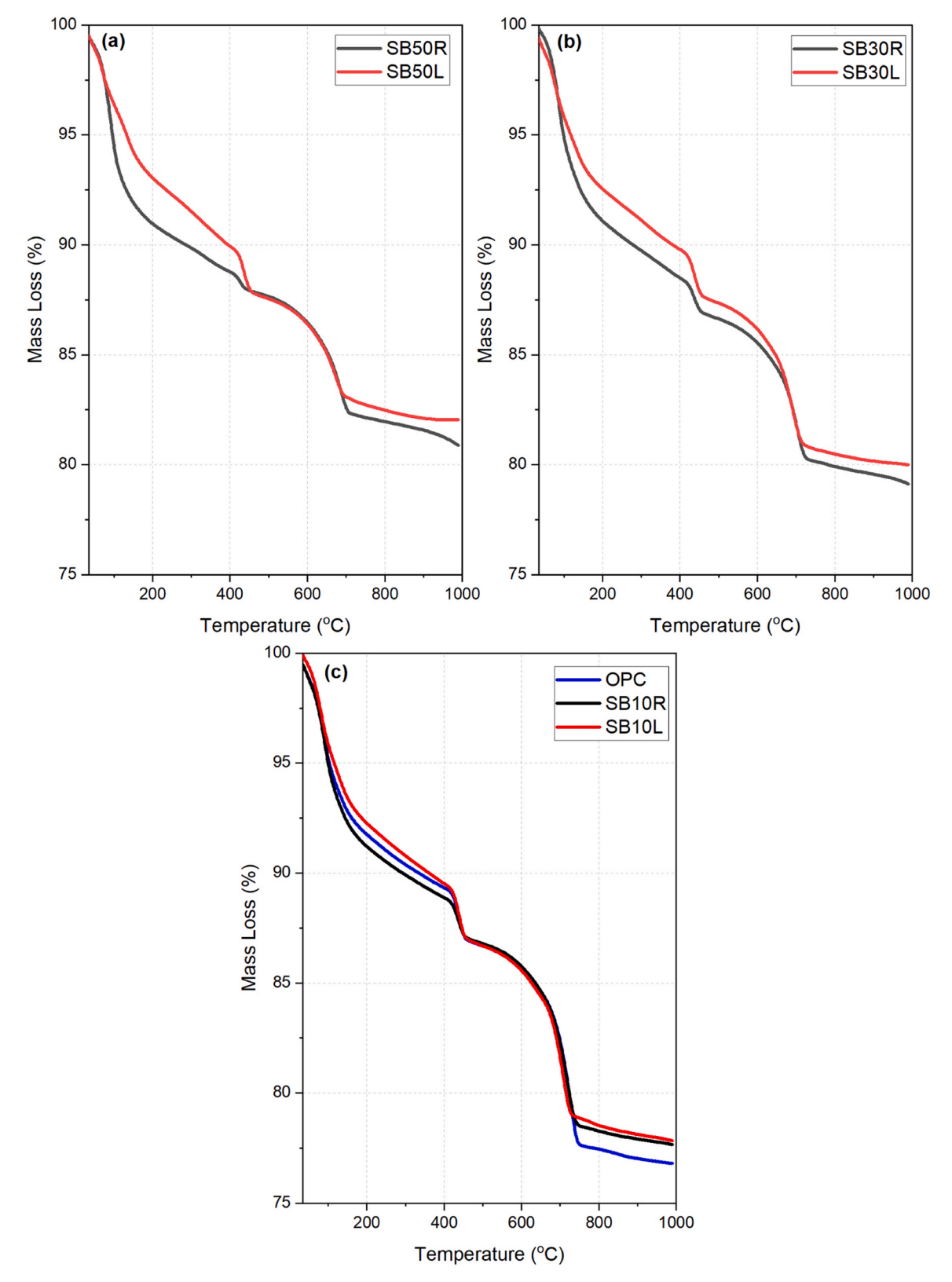


Fig. 18. TGA results for the investigated mix designs (a) SB50R and SB50L (b) SB30R and SB30L (c) SB10R, SB10L and OPC.

3.8. Chemical shrinkage

Fig. 20 presents volume change versus time during the first 24 hours of CBPD and OPC pastes. CBPD L caused significant expansion and experienced the greatest overall volume change, followed by CBPD R $\,$

and OPC. The expansion of CBPD L was fastest during the first five hours of curing, stabilising after that. Czapik et al. [14] also observed similar results where their 100 % CBPD mix achieved a 55 % volume expansion mostly within the first 10 hours.

Swelling of up to 0.091 ml/g was experienced in CBPD L. This large

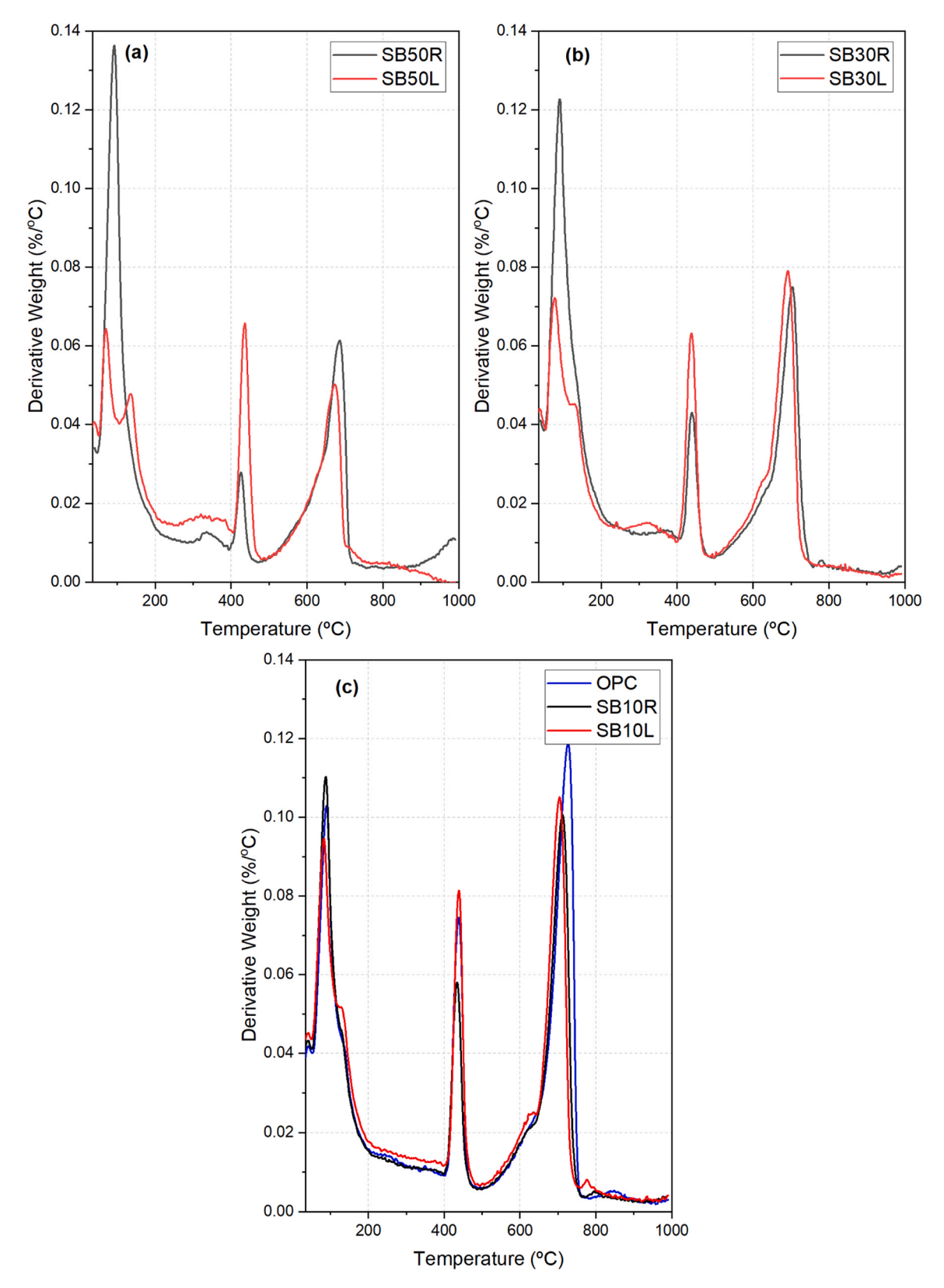


Fig. 19. DTG results for the investigated mix designs (a) SB50R and SB50L (b) SB30R and SB30L (c) SB10R, SB10L and OPC.

expansion is due to the CaO hydration that is highly exothermic enabling thermal expansion. The ratio of volume change of a CaO particle to a Ca (OH) $_2$ particle is circa 17/33 [49]. Excessive ettringite formation also causes expansion and likely the coupled effect of free lime hydration and ettringite formation lead to this swelling.

Though both CBPDs experienced eventual swelling, they did in a different manner. As observed from Fig. 21, CBPD R experienced shrinkage during the first 90 minutes before expanding. This indicates that there may be two factors that affect volume change in CBPD: ettringite formation and free lime hydration. It is possible that initially,

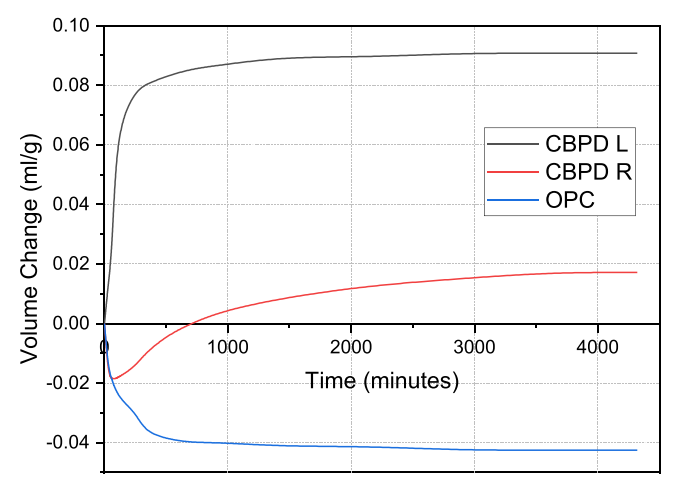


Fig. 20. CBPD R, CBPD L and OPC chemical shrinkage results.

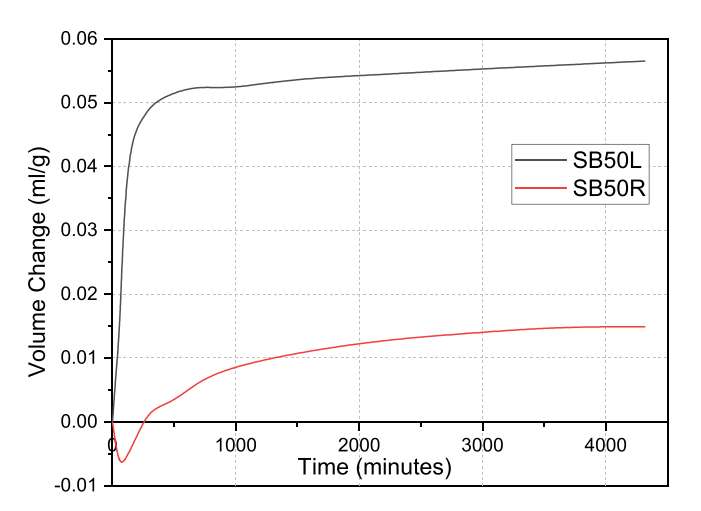


Fig. 21. SB50R and SB50L chemical shrinkage results.

CBPD R is shrinking, however as ettringite begins forming at early ages, it begins to expand. Overall, due to the compensating effect of shrinkage and swelling the volume change was the least with swelling of 0.018 ml/g by the end of testing. OPC only experienced shrinkage and had a result of $-0.043 \ ml/g$ by the end of testing.

The chemical shrinkage results for the mixes containing GBFS are shown Figs. 21–23. For SB50 mixes (Fig. 21) the expansion largely

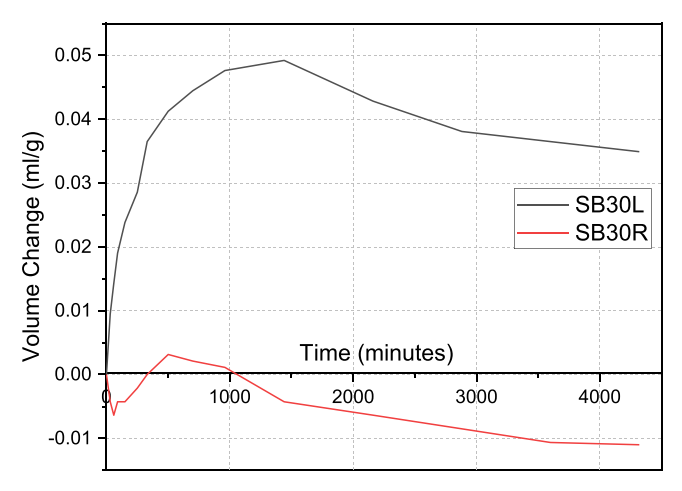


Fig. 22. SB30R and SB30L chemical shrinkage results.

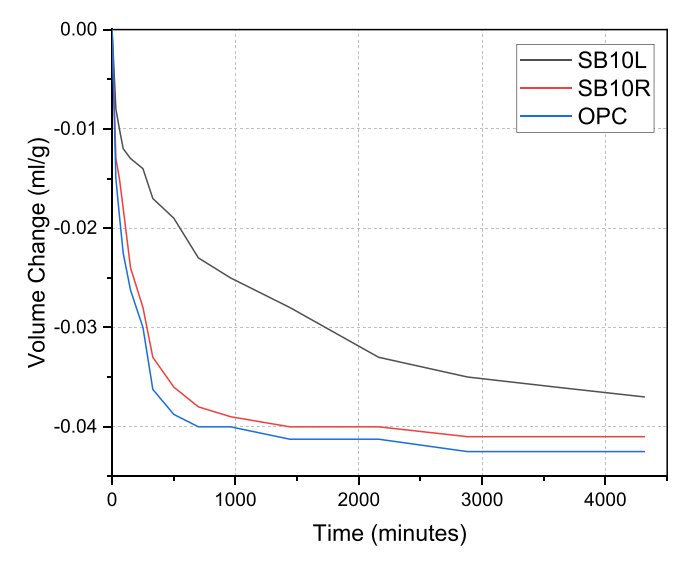


Fig. 23. SB10R, SB10L and OPC chemical shrinkage results.

follows the trend of the CBPD pastes, however, to a lesser degree. They both experience swelling where SB50R and SB50L experienced swelling of 0.015 ml/g and 0.057 ml/g, respectively after 3 days. Clearly the inclusion of GBFS inhibits the volume change, largely due to the slower reaction as seen in the heat of hydration results.

SB30R (Fig. 21) showed even lower volume change and it is evident that the expansion from the CBPD and the shrinkage from the cement are counteracting each other leading to an overall volume change $-0.011\ ml/g$. SB30L also experienced swelling, however to a lesser extent than before, clearly due to the reduced CBPD and increased cement content. Interestingly, after 48 hours, the paste started to shrink. This indicates that the CBPD L reacts at a much faster pace than cement. As the cement hydrates further, it induces shrinkage on the binder. SB30R experienced a similar effect, however to a lesser extent.

SB10 mixes showed shrinkage due to the high cement content (80 %), however SB10L showed a reduction in overall early age shrinkage relative to OPC. This is an interesting outcome that shows that CBPD has the potential to inhibit early age chemical shrinkage of cementitious binders.

3.9. Total shrinkage

Fig. 24 shows the total shrinkage for all samples up to 150 days. Final

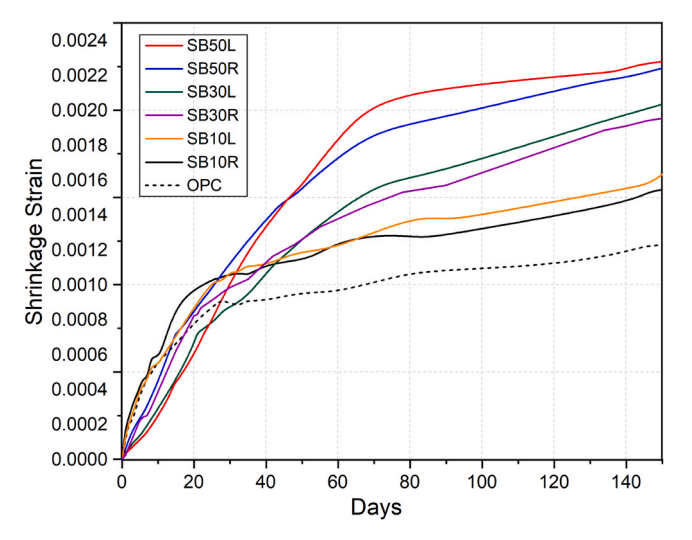


Fig. 24. Total shrinkage strains for all investigated mix designs.

total shrinkage increases with increasing content of CBPD.

At early ages up to 10 days, the shrinkage of both SB10 mixes and OPC is practically the same, due to the high OPC content. CBPD L binders somehow exhibits the capability to reduce early age-shrinkage, most notably observed in SB30L and SB50L with the lowest shrinkage up to 30 days. This indicates a direct effect of the initial chemical expansive behaviour on total drying shrinkage. This is likely due to the expansion during the formation of ettringite and the hydration of free lime which slowed down the overall shrinkage of these mixes. As this expansion slows down, CBPD mixes eventually exhibit higher shrinkage, surpassing that of OPC at later ages. This phenomenon was also observed in the chemical shrinkage, where SB30 binders expanded and then began shrinking after a few days. Future work should focus on the use of admixtures to reduce overall shrinkage. Shrinkage reducing admixtures have been effective in reducing drying shrinkage of GBFS based AAMs in previous research [50].

Another factor to consider is that the prisms were stored in ambient curing conditions. It has been found that expansion due to ettringite formation is greatly enhanced when cured in water and can take up to several months to complete. However, this is significantly reduced when stored in air, due to less access to water, and an increase in restraint [38]. It is likely that if water immersion shrinkage/expansion was monitored or the samples were cured for longer in water, the results would be very different and CBPD mixes would shrink less.

The type of CBPD clearly influences overall shrinkage, with CBPD R mixes consistently exhibiting lower shrinkage than their CBPD L counterparts by 90 days. However, mixes with the same CBPD quantity show similar trends, regardless of CBPD type. While the total shrinkage was highest by 150 days for SB50L, it should be noted that swelling did occur prior to the hardening of the paste with visible effect on the prisms. This may indicate that overall, the paste material expanded more than it shrunk. Total shrinkage values at 7, 28, 90, and 150 days are detailed in Table 7.

3.10. CBPD classification

From the results, the differences between the two types of CBPD investigated are clear. CBPD L has a higher free lime and chloride content as evidenced by the XRD diffractograms. This enabled it to have different properties such as expansive behaviour, high exothermic behaviour, and weaker binders overall due to reduced density and uneven hydration. A CBPD as such may be classified as lime rich and based on the strength results, should be limited to low controlled strength applications. As example of a low strength material CBPD L can be reused as would be as a backfilling material. Li et al., [51] developed a backfilling material composed of fly ash, gypsum and GBFS with strengths up to 6.5 MPa. CBPD L binders can also be reused in soil stabilisation. Low strength GBFS AAMs have been utilised in the past to stabilise hazardous arsenic-bearing tailings as an example [52].

CBPD R binders gained strengths largely due to their sulphate content, which facilitated the formation of ettringite, and the higher quantity of calcite. Thus, this CBPD can be classified as sulphate rich. The balance between sulphates and free lime in this binder allows it to be more appropriate for reuse in more structural applications due to its suitable strength. Further optimisation of the material, through milling and other methods could lead to a much stronger binder.

4. Conclusions

This paper compared two types of bypass dust as activators of CBPD and discussed their differences. The results provided information on the effect the composition of CBPD has in GBFS-based mortars. Two types of CBPD were analysed, a sulphate-rich CBPD (CBPD-R) and a lime-rich CBPD (CBPD L). The following conclusions can be drawn:

Table 7Total shrinkage at 7, 28, 90 and 150 days for all the investigated mix designs.

7 Days	28 Days	90 Days	150 days
0.031 %	0.108 %	0.197 %	0.225 %
0.016 %	0.093 %	0.213 %	0.228 %
0.025 %	0.096 %	0.156 %	0.195 %
0.019 %	0.085 %	0.165 %	0.203 %
0.048 %	0.105 %	0.129 %	0.155 %
0.046 %	0.102 %	0.137 %	0.163 %
0.048 %	0.091 %	0.109 %	0.123 %
	0.031 % 0.016 % 0.025 % 0.019 % 0.048 % 0.046 %	0.031 % 0.108 % 0.016 % 0.093 % 0.025 % 0.096 % 0.019 % 0.085 % 0.048 % 0.105 % 0.046 % 0.102 %	0.031 % 0.108 % 0.197 % 0.016 % 0.093 % 0.213 % 0.025 % 0.096 % 0.156 % 0.019 % 0.085 % 0.165 % 0.048 % 0.105 % 0.129 % 0.046 % 0.102 % 0.137 %

- CBPD R binders have a higher water demand than CBPD L, and produce stiffer mixes relative to CBPD L. Hence, the binders also set faster. The reduction of GBFS and CBPD content lead to a better flowability.
- CBPD L is much more reactive and has a higher heat of hydration relative to CBPD R. This is attributed to the highly exothermic reaction between lime and water.
- 3. CBPD R binders are denser than CBPD L binders, and lead to stronger binders. Inclusion of cement is overall beneficial for the strength, however the 20 % replacement of OPC with CBPD-GBFS provided the strongest binders both in flexure and compression.
- 4. Chemical shrinkage results show initial expansion for both CBPD L and R binders, however for different reasons. It is hypothesised that CBPD L expands due to the free lime reaction with water, whereas CBPD R expands due to ettringite formation. This expansion also leads to lower total shrinkage at early ages, however by 90 days CBPD binders show higher total shrinkage than OPC.
- 5. Microstructural analysis shows that CBPD L produces a much larger amount of portlandite than CBPD R, however CBPD R produces more ettringite due to its higher sulphate content. Ultimately, both hydration reactions are dominated by these phases. CBPD R also had a higher calcite content.

Overall, this research explained the reason for the differences in hydration with different types of CBPD, and what may be expected when dealing with these materials. Based on these results, it can be concluded that a CBPD that is lower in free lime content can be more favourable due to less overall expansion, leading to stronger binders and likely more durable mortar/concrete. At the end the CBPD was classified as sulphate or lime rich, and the potential uses of each type was highlighted. Future work should focus more on durability studies on CBPD binders as well as the use of admixtures to aid in workability and shrinkage of these binders.

CRediT authorship contribution statement

Ahmad Mahmoud Kobeiter Abiad: Writing – original draft, Methodology, Investigation, Formal analysis, Conceptualization. Hajime Kinoshita: Writing – review & editing, Supervision. Maurizio Guadagnini: Writing – review & editing, Supervision. Kypros Pilakoutas: Writing – review & editing, Supervision.

Declaration of Competing Interest

The authors declare the following financial interests/personal relationships which may be considered as potential competing interests: Ahmad Mahmoud Kobeiter Abiad reports financial support was provided by Engineering and Physical Sciences Research Council. If there are other authors, they declare that they have no known competing financial interests or personal relationships that could have appeared to influence the work reported in this paper.

Data availability

Data will be made available on request.

Acknowledgement

The corresponding author would like to thank the Engineering and Physical Sciences Research Council (EPSRC) for sponsoring his PhD studies.

Authors' declaration

The authors declare that there is no conflict of interest that may have influenced the work reported in this paper.

References

- P.C. Hewlett, Lea's chemistry of cement and concrete, Elsevier Science, San Diego, 2019.
- [2] Q. Zhang, P. Feng, X. Shen, J. Lu, S. Ye, H. Wang, T.C. Ling, Q. Ran, Utilization of solid wastes to sequestrate carbon dioxide in cement-based materials and methods to improve carbonation degree: a review, in: Journal of CO2 Utilization, Vol. 72, Elsevier Ltd, 2023, https://doi.org/10.1016/j.jcou.2023.102502.
- [3] X. Wang, J. Xu, Z. Wang, W. Yao, Use of recycled concrete aggregates as carriers for self-healing of concrete cracks by bacteria with high urease activity, Constr. Build. Mater. 337 (2022), https://doi.org/10.1016/j.conbuildmat.2022.127581.
- [4] M. Kazemian, B. Shafei, Carbon sequestration and storage in concrete: A state-of-the-art review of compositions, methods, and developments, in: Journal of CO2 Utilization, Vol. 70, Elsevier Ltd, 2023, https://doi.org/10.1016/j.icou.2023.102443.
- [5] B. Lothenbach, K. Scrivener, R.D. Hooton, Supplementary cementitious materials, Cem. Concr. Res. Vol. 41 (Issue 12) (2011) 1244–1256, https://doi.org/10.1016/j. cemconres.2010.12.001.
- [6] D. Coffetti, E. Crotti, L. Coppola, Long-term properties of self-cleaning alkaliactivated slag-based mortars with titanium dioxide nanoparticles, Constr. Build. Mater. 392 (2023), https://doi.org/10.1016/j.conbuildmat.2023.131976.
- [7] A.N. Derinpinar, M.B. Karakoç, A. Özcan, Performance of glass powder substituted slag based geopolymer concretes under high temperature, Constr. Build. Mater. 331 (2022), https://doi.org/10.1016/j.conbuildmat.2022.127318.
- [8] V. Revilla-Cuesta, R. Serrano-López, A.B. Espinosa, V. Ortega-López, M. Skaf, Analyzing the relationship between compressive strength and modulus of elasticity in concrete with ladle furnace slag, Buildings 13 (12) (2023), https://doi.org/ 10.3390/buildings13123100.
- [9] V. López-Ausín, V. Revilla-Cuesta, M. Skaf, V. Ortega-López, Mechanical properties of sustainable concrete containing powdery ladle furnace slag from different sources, Powder Technol. 434 (2024), https://doi.org/10.1016/j. powtec.2024.119396.
- [10] T. Cakmak, I. Ustabas, Z. Kurt, E. Yilmaz, Geopolymer mortars having glassy materials considering mechanical and microstructural features, J. Build. Eng. 91 (2024), https://doi.org/10.1016/j.jobe.2024.109738.
- [11] E. Kravchenko, G. Lazorenko, X. Jiang, Z. Leng, Alkali-activated materials made of construction and demolition waste as precursors: A review, in: Sustainable Materials and Technologies, Vol. 39, Elsevier B.V, 2024, https://doi.org/10.1016/ j.susmat.2024.e00829.
- [12] M.F. Alnahhal, T. Kim, A. Hajimohammadi, Waste-derived activators for alkaliactivated materials: a review, Cem. Concr. Compos. 118 (2021), https://doi.org/ 10.1016/j.cemconcomp.2021.103980.
- [13] D. Barnat-Hunek, J. Góra, Z. Suchorab, G. Łagód, Cement kiln dust. Waste and Supplementary Cementitious Materials in Concrete: Characterisation, Properties and Applications, Elsevier, 2018, pp. 149–180, https://doi.org/10.1016/B978-0-08-102156-9.00005-5.
- [14] P. Czapik, J. Zapała-Sławeta, Z. Owsiak, P. Stępień, Hydration of cement by-pass dust, Constr. Build. Mater. 231 (2020), https://doi.org/10.1016/j. conbuildmat.2019.117139.
- [15] W. Adaska, D. Taubert, Beneficial Uses Of Cement Kiln Dust, IEEE-IAS Cement Industry Committee, Miami, Florida, 2008.
- [16] W. Hu, W.C. Cheng, Y. Wang, S. Wen, Feasibility study of applying a graphene oxide-alginate composite hydrogel to electrokinetic remediation of Cu(II)contaminated loess as electrodes, Sep. Purif. Technol. 322 (2023), https://doi.org/ 10.1016/j.seppur.2023.124361.
- [17] W. Hu, W.C. Cheng, S. Wen, N. Kang, Revealing underlying mechanisms affecting electrokinetic remediation of an artificially Cu- and Pb-contaminated loess using the external regulatory system with adsorbent, Front. Mater. 9 (2022), https://doi. org/10.3389/fmats.2022.967871.
- [18] T. Hanein, Y. Hayashi, C. Utton, M. Nyberg, J.C. Martinez, N.I. Quintero-Mora, H. Kinoshita, Pyro processing cement kiln bypass dust: enhancing clinker phase formation, Constr. Build. Mater. 259 (2020), https://doi.org/10.1016/j. conbuildmat.2020.120420.
- [19] N. Tkachenko, K. Tang, M. McCarten, S. Reece, D. Kampmann, C. Hickey, M. Bayaraa, P. Foster, C. Layman, C. Rossi, K. Scott, D. Yoken, C. Christiaen, B. Caldecott, Global database of cement production assets and upstream suppliers, Sci. Data 10 (1) (2023), https://doi.org/10.1038/s41597-023-02599-w.
- [20] P. Chaunsali, S. Peethamparan, Influence of the composition of cement kiln dust on its interaction with fly ash and slag, Cem. Concr. Res. 54 (2013) 106–113, https:// doi.org/10.1016/j.cemconres.2013.09.001.

- [21] M. Sadique, E. Coakley, The influence of physico-chemical properties of fly ash and CKD on strength generation of high-volume fly ash concrete, Adv. Cem. Res. 28 (2016) 595–605, https://doi.org/10.1680/jadcr.15.00103.
- [22] K. Wojtacha-Rychter, M. Król, M. Gołaszewska, J. Całus-Moszko, M. Magdziarczyk, A. Smoliński, Dust from chlorine bypass installation as cementitious materials replacement in concrete making, J. Build. Eng. 51 (2022), https://doi.org/ 10.1016/i.jobe.2022.104309.
- [23] M.S. Konsta-Gdoutos, S.P. Shah, Hydration and properties of novel blended cements based on cement kiln dust and blast furnace slag, Cem. Concr. Res. 33 (8) (2003) 1269–1276, https://doi.org/10.1016/S0008-8846(03)00061-9.
- [24] K.A.M. ElNaggar, M.M. Ahmed, W. Abbas, E.M. Abdel Hamid, Recycling of bypass cement kiln dust in the production of eco-friendly roof tiles, Mater. Res. Express 10 (6) (2023), https://doi.org/10.1088/2053-1591/acddb9.
- [25] S.K. Adekunle, Carbon sequestration potential of cement kiln dust: Mechanisms, methodologies, and applications, in: Journal of Cleaner Production, Vol. 446, Elsevier Ltd, 2024, https://doi.org/10.1016/j.jclepro.2024.141283.
- [26] L. Senff, J.A. Labrincha, V.M. Ferreira, D. Hotza, W.L. Repette, Effect of nano-silica on rheology and fresh properties of cement pastes and mortars, Constr. Build. Mater. 23 (7) (2009) 2487–2491, https://doi.org/10.1016/j. conbuildmat 2009 02 005
- [27] S.U. Khan, M.F. Nuruddin, T. Ayub, N. Shafiq, Effects of different mineral admixtures on the properties of fresh concrete, in: The Scientific World Journal, Vol. 2014, ScientificWorld Ltd, 2014, https://doi.org/10.1155/2014/986567.
- [28] T.H.F. W, Cement Chemistry, Thomas Telford, London, 1997.
- [29] G.H. Cai, Y.F. Zhou, J.S. Li, L.J. Han, C.S. Poon, Deep insight into mechanical behavior and microstructure mechanism of quicklime-activated ground granulated blast-furnace slag pastes, Cem. Concr. Compos. 134 (2022), https://doi.org/ 10.1016/j.cemconcomp.2022.104767.
- [30] M. Zhu, G. Xie, L. Liu, R. Wang, S. Ruan, P. Yang, Z. Fang, Strengthening mechanism of granulated blast-furnace slag on the uniaxial compressive strength of modified magnesium slag-based cemented backfilling material, Process Saf. Environ. Prot. 174 (2023) 722–733, https://doi.org/10.1016/j.psep.2023.04.031.
- [31] I. Özkan, Z. Yayla, Evaluation of correlation between physical properties and ultrasonic pulse velocity of fired clay samples, Ultrasonics 66 (2016) 4–10, https:// doi.org/10.1016/j.ultras.2015.12.008.
- [32] P. Chaunsali, S. Peethamparan, Novel cementitious binder incorporating cement kiln dust: strength and durability, Acids Mater. J. 110 (3) (2013) 297–304, https://doi.org/10.14359/51685663.
- [33] E. Gallucci, X. Zhang, K.L. Scrivener, Effect of temperature on the microstructure of calcium silicate hydrate (C-S-H), Cem. Concr. Res. 53 (2013) 185–195, https://doi. org/10.1016/j.cemconres.2013.06.008.
- [34] Y. Gu, O. Omikrine Metalssi, R.P. Martin, T. Fen-Chong, P. Dangla, Locating ettringite due to DEF at the pore scale of cement paste by heat-based dissolution tests, Constr. Build. Mater. 258 (2020), https://doi.org/10.1016/j. conbuildmat.2020.120000.
- [35] S. von Greve-Dierfeld, B. Lothenbach, A. Vollpracht, B. Wu, B. Huet, C. Andrade, C. Medina, C. Thiel, E. Gruyaert, H. Vanoutrive, I.F. Saéz del Bosque, I. Ignjatovic, J. Elsen, J.L. Provis, K. Scrivener, K.C. Thienel, K. Sideris, M. Zajac, N. Alderete, N. De Belie, Understanding the carbonation of concrete with supplementary cementitious materials: a critical review by RILEM TC 281-CCC, Mater. Struct. /Mater. Et. Constr. 53 (6) (2020), https://doi.org/10.1617/s11527-020-01558-w.
- [36] M.T. Marvila, J. Alexandre, A.R.G. de Azevedo, E.B. Zanelato, Evaluation of the use of marble waste in hydrated lime cement mortar based, J. Mater. Cycles Waste Manag. 21 (5) (2019) 1250–1261, https://doi.org/10.1007/s10163-019-00878-6.
- [37] S. Chakraborty, B.W. Jo, M.A. Sikandar, Hydration mechanism of the hydrogenrich water based cement paste, J. Phys. Chem. C. 120 (2016) 8198–8209, https:// doi.org/10.1021/acs.jpcc.6b01444.
- [38] Ghorab, H.Y. (2004). On the chemistry of delayed ettringite formation. International RILEM Workshop on Internal Sulfate Attack and Delayed Ettringite Formation [Preprint]. https://doi:\langle 10.1617/2912143802.005 \rangle.
- [39] J. Havlica, S. Sahu, Mechanism of ettringite and monosulphate formation, Cem. Concr. Res. Vol. 22 (1992), https://doi.org/10.1016/0008-8846(92)90019-R.
- [40] E. Bernard, B. Lothenbach, C. Cau-Dit-Coumes, C. Chlique, A. Dauzères, I. Pochard, Magnesium and calcium silicate hydrates, Part I: investigation of the possible magnesium incorporation in calcium silicate hydrate (C-S-H) and of the calcium in magnesium silicate hydrate (M-S-H), Appl. Geochem. 89 (2018) 229–242, https:// doi.org/10.1016/j.apgeochem.2017.12.005.
- [41] B. wan Jo, S. Chakraborty, J.H. Jo, Effectiveness of a hydrothermally produced alternative cementitious material on the physical and mechanical performance of concrete (https://doi:), J. Clean. Prod. 142 (2017) 3269–3280, https://doi.org/ 10.1016/j.jclepro.2016.10.142.
- [42] P. Yu, et al., Structure of calcium silicate hydrate (c-s-h): near-, mid-, and far-infrared spectroscopy (https://doi.), J. Am. Ceram. Soc. 82 (3) (1999) 742–748, https://doi.org/10.1111/j.1151-2916.1999.tb01826.x.
- [43] Y. Yan, B. Ma, G.D. Miron, D.A. Kulik, K. Scrivener, B. Lothenbach, Al uptake in calcium silicate hydrate and the effect of alkali hydroxide, Cem. Concr. Res. 162 (2022), https://doi.org/10.1016/j.cemconres.2022.106957.
- [44] E. Scholtzová, L. Kucková, J. Kožíšek, D. Tunega, Structural and spectroscopic characterization of ettringite mineral -combined DFT and experimental study, J. Mol. Struct. 1100 (2015) 215–224, https://doi.org/10.1016/j. molstruc 2015 06 075
- [45] T. Shi, Y. Gao, D.J. Corr, S.P. Shah, FTIR study on early-age hydration of carbon nanotubes-modified cement-based materials, Adv. Cem. Res. 31 (8) (2019) 353–361, https://doi.org/10.1680/jadcr.16.00167.
- [46] M.S.M. Basri, F. Mustapha, N. Mazlan, M.R. Ishak, Rice husk ash-based geopolymer binder: compressive strength, optimize composition, FTIR spectroscopy,

- microstructural, and potential as fire-retardant material \dagger , Polymers 13 (24) (2021) https://doi.org/10.3390/polym13244373.
- [47] D.N. Huntzinger, J.S. Gierke, S.K. Kawatra, T.C. Eisele, L.L. Sutter, Carbon dioxide sequestration in cement kiln dust through mineral carbonation, Environ. Sci. Technol. 43 (6) (2009) 1986–1992, https://doi.org/10.1021/es802910z.
- [48] Z. Zhou, M. Sofi, E. Lumantarna, R.S. Nicolas, G.H. Kusuma, P. Mendis, Strength development and thermogravimetric investigation of high-volume fly ash binders, Materials 12 (20) (2019), https://doi.org/10.3390/ma12203344.
- [49] W. Kurdowski, A. Thiel, On the role of free calcium oxide in expansive cements, Cem. Concr. Res.: Vol. Ii. (1981), https://doi.org/10.1016/0008-8846(81)90006-5.
- [50] L. Coppola, D. Coffetti, E. Crotti, S. Candamano, F. Crea, G. Gazzaniga, T. Pastore, The combined use of admixtures for shrinkage reduction in one-part alkali activated slag-based mortars and pastes, Constr. Build. Mater. 248 (2020), https://doi.org/10.1016/j.conbuildmat.2020.118682.
- [51] J. Li, S. Cao, E. Yilmaz, Characterization of macro mechanical properties and microstructures of cement-based composites prepared from fly ash, gypsum and steel slag, Minerals 12 (1) (2022), https://doi.org/10.3390/min12010006.
- [52] H. Jiang, J. Zheng, Y. Fu, Z. Wang, E. Yilmaz, L. Cui, Slag-based stabilization/ solidification of hazardous arsenic-bearing tailings as cemented paste backfill: strength and arsenic immobilization assessment, Case Stud. Constr. Mater. 20 (2024), https://doi.org/10.1016/j.cscm.2024.e03002.